



Hydrocarbon mixture and CO₂ adsorptions in A nanopore-bulk multiscale system in relation to CO₂ enhanced shale gas recovery

Yingnan Wang, Zhehui Jin *

School of Mining and Petroleum Engineering, Department of Civil and Environmental Engineering, University of Alberta, Edmonton, AB T6G 1H9, Canada

ARTICLE INFO

Keywords:

Shale gas
CO₂ 'huff-n-puff'
Nanopores
Enhanced gas recovery
CO₂ sequestration

ABSTRACT

Thanks to the continuous depletion of conventional gas reservoirs, shale gas plays an important role to meet the global natural gas demand. The CO₂ 'huff-n-puff' process has been proven to be an effective method to enhance shale gas recovery and sequester CO₂. Unlike conventional reservoirs, shale media can contain a significant number of nano-scaled pores and their pore volume can be comparable to that of macropores and fractures in which fluids behave as bulk. While previous works studied the mechanisms of CO₂ 'huff-n-puff' process in shale gas exploitation, the volume partitioning between nanopores and macropores/fractures is not fully taken into account. In this work, we built a nanopore-bulk multiscale model with varying pore size distributions (PSDs) to study the CO₂ 'huff-n-puff' process in a constant volume depletion (CVD) setting by using density functional theory (DFT). We found that the volume partitioning effect on adsorption, fluid compositions, hydrocarbon mixture (C₁, C₂, and C₃) recovery is significant in the CO₂ 'huff-n-puff' process. The majority of hydrocarbon mixtures can be released from micropores and smaller mesopores during the CO₂ 'huff' and 'soak' process, while the average hydrocarbon densities in larger mesopores might increase. During the CO₂ 'huff' and 'soak' process, due to a stronger confinement effect in smaller pores, the PSD case with a higher volume ratio of smaller pores releases fewer hydrocarbons, while stores more CO₂ per unit pore volume. Overall, the volume partitioning has a significant effect on hydrocarbon adsorption, compositions, and recovery as well as CO₂ storage during the CO₂ 'huff-n-puff' process in shale gas exploitation and geological CO₂ sequestration.

1. Introduction

Thanks to the continuous depletion of conventional gas reservoirs [1] and the growing global energy demand [2], shale gas has become an important natural gas supply. Due to the presence of a significant amount of nanosized pores [3] shale media is associated with ultra-low permeability and porosity [4–6]. In contrast to the conventional gas reservoirs, in shale media, surface adsorption plays a dominant role in total gas uptake and estimation of the gas-in-place (GIP) [7]. On the other hand, based on the field data [8], shale gas production rates generally plummet rapidly which greatly hampers its exploitation and development activities. In fact, the average recovery efficiency of shale gas is less than 10%, if only horizontal and hydraulic fracturing methods are implemented [9]. As an enhanced gas recovery (EGR) method, CO₂ injection has been proven to be an effective method to drive up shale gas production rate by up to 8 times [8]. Additionally, considering abundant storage capacity and the readily-available underground as well as surface infrastructures [10,11], CO₂ injection into shale gas reservoirs can

be a viable option to alleviate carbon emissions through geological CO₂ sequestrations (GCSs) [12,13].

During the CO₂-EGR process in shale gas exploitation, CO₂ 'huff-n-puff' is one of the most widely used methods [8,14–16] which can be generally separated into CO₂ injection ('huff'), well shut-in ('soak'), and production ('puff') periods [17,18]. There have been a few experimental measurements on gas adsorption in shale and CO₂ 'huff-n-puff' process [19–22]. Holmes *et al.* [19] conducted experimental measurements to study N₂ and Ar uptake in pure organic/inorganic components (kerogen, silica, calcite, and illite), idealized (*i.e.*, mixing different pure components), and actual shale samples. They observed that organic matter shows a stronger adsorption capacity than inorganic matters. In idealized shale samples, for a given clay content, adsorption capacity has a linear correlation with total organic carbon content (TOC), while for a given TOC, adsorption amount also increases as clay content increases. On the other hand, gas uptake in actual shale samples generally increases as TOC increases. Liu *et al.* [20,21] used the low-field nuclear magnetic resonance (NMR) spectroscopy to quantitatively identify the

* Corresponding authors.

E-mail address: zhehui2@ualberta.ca (Z. Jin).

<https://doi.org/10.1016/j.cej.2020.128398>

Received 22 October 2020; Received in revised form 24 December 2020; Accepted 30 December 2020

Available online 14 February 2021

1385-8947/© 2021 Elsevier B.V. All rights reserved.

Table 1

Volume ratios and absolute volume in the nanopore-bulk multiscale systems of PSDs from the Eagle Ford (EF) [71], Middle Bakken (MB) [73], and Horn River (HR) [72] shale sub-formations. In our modeling, all PSDs have the same total pore volume as 1 m^3 .

		Nanopores				Bulk
		2nm	5nm	15nm	30nm	
Volume ratio (%)	EF	11.50	27.50	12.00	18.00	31.00
	MB	2.87	15.00	33.38	34.53	14.22
	HR	0.48	2.59	4.61	20.73	71.59
Absolute volume (m^3)	EF	0.115	0.275	0.12	0.18	0.31
	MB	0.0287	0.15	0.3338	0.3453	0.1422
	HR	0.0048	0.0259	0.0461	0.2073	0.7159

adsorbed, pore-medium-confined, and free C_1 during pressure drawdown and CO_2 'huff-n-puff' process under simplified laboratory conditions at 35°C . They found that the desorption efficiency of adsorbed C_1 is enhanced by $\sim 26\%$ due to CO_2 injection. On the other hand, numerical simulations have been widely used to investigate CO_2 'huff-n-puff' process for shale gas recovery and CO_2 sequestration [23–25]. Xu *et al.* [23] studied the performance of CO_2 'huff-n-puff' in a triple-porosity dual-permeability shale model by considering gas adsorption/desorption, competitive adsorption, and binary gas diffusion. They found that the supercritical CO_2 'huff-n-puff' can increase shale gas recovery by 15%. Their simulation results also revealed that gas production rate and ultimate recovery would be higher for a higher total organic carbon (TOC) content. Kim *et al.* [24] assessed the performance of CO_2 'huff-n-puff' in three different shale formations by multi-component numerical simulations. They reported that the CO_2 'huff-n-puff' enhances C_1 production by 6% in the Barnett shale, while it is less effective in the other two shale models due to different shale rock properties. Although these numerical simulations can reveal the effect of CO_2 injection on shale gas recovery and GCS, the underlying mechanisms governing these phenomena occurring in nanoporous media, such as competitive adsorption and compositional changes during CO_2 injection, remain largely ambiguous.

In this context, molecular simulations and theoretical modeling have also been applied to study CO_2 'huff-n-puff' performance in shale gas recovery and GCS from molecular perspectives [7,26–33]. Yuan *et al.* [27] studied the enhanced recovery, adsorption energy, and configuration of C_1 - CO_2 mixtures in carbon nanotubes (CNT) by molecular dynamics (MD) simulations. They found that the pre-adsorbed C_1 can be displaced by CO_2 injection in CNT and the recovery of C_1 is enhanced by more than 15%. Zhou *et al.* [30,31] studied pure and hydrocarbon mixture recovery during CO_2 'huff-n-puff' in kerogen micro-/mesopores by GCMC simulations. They explicitly investigated the effect of moisture content, pore size, and injection cycles. They found that during pressure drawdown, while C_1 in the adsorption layer and the middle of the pores can be recovered, C_3 can only be recovered in the middle of the pores. On the other hand, the injected CO_2 can recover hydrocarbons in the adsorption layer. Zhang *et al.* [32] studied the recovery mechanisms of C_1 - C_2 - C_3 mixtures in organic and inorganic micro-/mesopores during the CO_2 'huff-n-puff' process. They revealed that CO_2 'huff' and 'soak' is more efficient in organic micro-/mesopores in terms of hydrocarbon recovery, especially for the heavier component (C_3). During CO_2 injection, CO_2 storage in micro-/mesopores is mainly by displacing hydrocarbons from the micro-/mesopores, while dominating in the first adsorption layers. Bakhshian *et al.* [33] used a lattice-based density functional theory to study CO_2 adsorption-induced deformation in shale micro-/mesopores. They observed stronger adsorption in duct pores comparing to slit pores and a sharp rise in adsorption isotherm as well as swelling strain at conditions close to the bulk critical point of CO_2 . While these molecular simulations and theoretical studied CO_2 -EGR and CO_2 sequestration from molecular perspectives, they generally assume that the bulk phase volume is much larger than that of nanopores so that the

fluid injection into and release from the nanopores do not alter the fluid compositions in bulk.

However, in shale reservoirs, the pore volume in nanopores can be comparable to that of macropores/fractures [34,35] and the volume partitioning among nanopores and macropores/fractures (bulk) plays an important role in fluid properties and phase behaviors [36–40]. Due to the comparable pore volume, adsorbed/released fluids in/from nanopores could influence bulk fluid properties, which in turn could further affect fluid density distributions in nanopores through chemical equilibrium [31,32,41,42]. A few works incorporated such a nanopore-bulk multiscale system to study properties of pure and hydrocarbon mixtures [36,38–40,43–45]. They generally show that hydrocarbon mixture phase behaviors in the nanopore-bulk multiscale system are different from those in the systems with infinitely large bulk reservoirs. Thus, to simulate the hydrocarbons recovery process in shale reservoirs, a constant volume depletion (CVD) method can be implemented. In our previous work [37] we studied the effect of volume partitioning on hydrocarbon mixture adsorption in three different shale samples in a CVD setting by using engineering DFT. We found that due to the volume partitioning, the bulk fluid composition keeps changing during the pressure drawdown process and the released hydrocarbon properties are dependent on pore size distribution (PSD). However, to the best of our knowledge, the effect of volume partitioning on CO_2 -EGR and CO_2 sequestration during the CO_2 'huff-n-puff' process has not been revealed yet.

Thus, in this work, we explicitly study the effect of volume partitioning on hydrocarbon mixtures and CO_2 adsorption in shale nanoporous media during the CO_2 'huff-n-puff' process. Kerogen is the main constituent of organic matter in shale, which greatly contributes to the total GIP [29,46–48]. For simplicity, in this work, we use carbon slit nanopores [42,49–51] to represent kerogen nanopores, which have shown a good agreement with experimental measurements on gas adsorption in kerogen nanoporous media [52–54]. We note that the nanopores consist of micropores ($<2 \text{ nm}$) and mesopores ($2\text{--}50 \text{ nm}$) [55] while macropores ($\geq 50 \text{ nm}$) are treated as bulk region, as fluid properties in macropores are similar to those in bulk [56,57]. Three different PSD cases based on characterizations of shale sub-formations are considered in a CVD setting, in which nanopore volume is comparable to that in the bulk region. By using perturbed-chain-statistical-associating-fluid-theory-based DFT (PC-SAFT DFT) [58–60], which has shown an excellent agreement with experimental measurements and molecular simulations in terms of fluid adsorption characteristics [59–69], hydrocarbon mixtures and CO_2 adsorption, their density distributions, and average densities in nanopores can be explicitly calculated. On the other hand, in contrast to molecular simulations, PC-SAFT DFT can significantly reduce the calculation time [62–65,70]. During the primary pressure drawdown and the CO_2 'puff' processes, hydrocarbon mixtures and CO_2 are depleted from the nanopore-bulk multiscale system by the CVD method, while during the CO_2 'huff' and 'soak' process, CO_2 is injected without any fluid recovered from the entire system. Our work should provide fundamental understandings about the

Table 2
Initial bulk mole fractions for C₁-C₂-C₃ mixtures in different PSDs.

	C ₁	C ₂	C ₃	Sum
Eagle Ford	0.85	0.15	0.05	1
Middle Bakken	0.85	0.15	0.05	1
Horn River	0.85	0.15	0.05	1

effect of volume partitioning on hydrocarbon mixtures and CO₂ adsorption characteristics and important insights into shale gas exploitations and GCS during the CO₂ 'huff-n-puff' process.

2. Model and methodology

2.1. Nanopore-bulk multiscale system

The nanopore-bulk multiscale system consists of two distinct parts: nanopores and the bulk region [37]. The bulk region may refer to hydraulic/natural fractures as well as macropores in the shale matrix. Similar to our previous work [37], we assume that hydrocarbon mixtures and CO₂ in pores larger than 50 nm behave as bulk. On the other hand, pores of size smaller than 50 nm are treated as nanopores in which fluid-surface interactions are explicitly considered. Based on the PSDs from Eagle Ford (EF) [71], Horn River (HR) [72], and Middle Bakken (MB) [73] shale sub-formation characterizations, four distinct pores are used to represent micropores and mesopores in shale: 2 nm (≤2 nm), 5 nm (2–10 nm), 15 nm (10–20 nm), and 30 nm (20–50 nm) [37]. The pore volume fractions in each nanopore and the bulk region are shown in Table 1. In our model, the pressure P is dictated by the fluid pressure in the bulk region. While the chemical potential of each component in nanopores is the same as that in bulk at equilibrium, we do not consider the interfaces between nanopores and bulk region. It has been shown that the mechanical equilibrium between nanopores and bulk is always automatically satisfied by the equality of chemical potentials [74].

2.2. Material balance

In this work, material balance calculation is necessary for 1) primary pressure drop; 2) CO₂ 'huff' and 'soak'; 3) CO₂ 'puff' processes. During the CVD process, the bulk region volume is expanded to lower the bulk pressure, while the fluids in the excess bulk volume are removed from the entire system [40]. The system temperature is fixed at 333.15 K with an initial pressure $P_0 = 500$ bar, which can represent typical shale gas reservoir temperature and pressure [13,75,76]. C₁-C₂-C₃ mixtures are used to represent hydrocarbon mixtures and the initial bulk compositions for three different PSD cases are listed in Table 2. The initial mole fraction of component k in the entire system, X_k^{init} , at P_0 is given as

$$X_k^{init}(P_0) = \frac{m_k^{init}(P_0)}{\sum_{k=C_1,C_2,C_3} m_k^{init}(P_0)}, \quad k = C_1, C_2, C_3, \quad (1)$$

with

$$m_k^{init}(P_0) = \rho_{k,b}^{init}(P_0)V_b + \sum_W \rho_{ave,k,W}^{init}(P_0)V_{p,W}, \quad k = C_1, C_2, C_3, \quad (2)$$

where $V_{p,W}$ is the pore volume of the nanopore of W , V_b is the bulk volume. In this work, we set the entire system volume identical for all three PSD cases as 1 m^3 . The pore and bulk volume, as well as their volume ratios, are listed in Table 1. $\rho_{k,b}^{init}(P_0)$ and $\rho_{ave,k,W}^{init}(P_0)$ are molar density of component k in bulk and average molar density of component k in nanopore of W at P_0 , respectively, $m_k^{init}(P_0)$ is the total mole number of component k at P_0 . While $\rho_{k,b}^{init}(P_0)$ is obtained from the PC-SAFT equation of state (EOS) at P_0 , $\rho_{ave,k,W}^{init}(P_0)$ is obtained from the PC-

Table 3

Injected CO₂ amount and its molar ratio in the total system at $P_1 = 100$ bar in each PSD.

	Injected CO ₂	
	Absolute amount (mol)	Molar ratio in system
Eagle Ford	2379.58	27.1%
Middle Bakken	2379.58	30.0%
Horn River	2379.58	33.9%

SAFT DFT.

During the CVD process, $V_{p,W}$ does not change but V_b expands as P decreases, and the fluids in the excess bulk volume are then removed. The material balance is applied to calculate the expanded bulk volume $V_{k,b}^o(P)$ based on component k before fluid removal at given P and the removed fluid $m_k^{re}(P)$ of component k in the excess bulk volume,

$$V_{k,b}^o(P) = \frac{m_k^o(P) - \sum_W \rho_{ave,k,W}(P)V_{p,W}}{X_{k,b}(P)\rho_b(P)}, \quad k = C_1, C_2, C_3, \quad (3)$$

$$m_k^{re}(P) = [V_b^o(P) - V_b]\rho_{k,b}(P), \quad k = C_1, C_2, C_3, \quad (4)$$

where $m_k^o(P)$ is the total mole number of component k at P before removal; $\rho_{ave,k,W}(P)$ and $\rho_b(P)$ are average molar density of component k in nanopore of W and molar density of component k in bulk at P , respectively; $X_{k,b}(P)$ refers to the mole fraction of component k in bulk at P . An iterative method is used to find the bulk mole fraction $\{X_{k,b}(P)\}$, which satisfies that $V_{k,b}^o(P)$ converge at the actual expanded bulk volume $V_b^o(P)$. Thus, the remaining fluids in the entire system $m_k^r(P)$ of component k at P are given as

$$m_k^r(P) = m_k^o(P) - m_k^{re}(P), \quad k = C_1, C_2, C_3. \quad (5)$$

Then, $m_k^r(P)$ serves as m_k^o at the subsequent pressure condition. In each step, we lower P by 2 bar in all PSD cases until $P_1 = 100$ bar, which is a typical CO₂ injection pressure in the fields [8,15,25,77,78].

Then, the CO₂ 'huff' and 'soak' process during which bulk fluids and those in nanopores reach chemical equilibrium after CO₂ injection is initiated by injecting an equal amount of CO₂ in each PSD case as listed in Table 3. We note that in this process, both bulk and nanopore volumes remain unchanged and no fluids are released from the entire system. Due to CO₂ injection, the bulk pressure is elevated to a higher pressure P_2 , while the bulk composition is altered. To find the equilibrium bulk composition and pressure, the materials balance equations are solved, which are given as,

$$\begin{cases} m_k(P_2) = m_k(P_1) = \rho_{k,b}(P_2)V_b + \sum_W \rho_{ave,k,W}(P_2)V_{p,W}, \quad k = C_1, C_2, C_3 \\ m_{CO_2}(P_2) = m_{CO_2}^{inj}(P_1) = \rho_{CO_2,b}(P_2)V_b + \sum_W \rho_{ave,CO_2,W}(P_2)V_{p,W} \\ \sum_{k=C_1,C_2,C_3} X_{k,b}(P_2) + X_{CO_2,b}(P_2) = 1 \end{cases} \quad (6)$$

where $m_k(P_1)$ and $m_k(P_2)$ are the total mole number of component k in the entire system at P_1 and P_2 , respectively; $m_{CO_2}^{inj}(P_1)$ is the total mole number of injected CO₂ at P_1 ; $m_{CO_2}(P_2)$ is the total mole number of CO₂ in the entire system at P_2 . The bulk composition and pressure are obtained by solving Eq. (6) iteratively. The equilibrium bulk pressures and compositions in each PSD case are listed in Table 4.

During the CO₂ 'puff' process, the pressure continues to decrease from P_2 . The bulk volume expands and fluids released from the entire system during the CO₂ 'puff' process as pressure drops. The material

Table 4

Bulk pressure, composition, and densities of hydrocarbons and CO₂ in various PSD cases before and after CO₂ 'huff' and 'soak' processes. Note that the $\Delta P_{b, after}$ is

defined as $\Delta P_{b, after} = \frac{|\bar{P}_{b, after} - P_{b, after}|}{\bar{P}_{b, after}} \times 100\%$, where $P_{b, after}$ and $\bar{P}_{b, after}$ are bulk pressure for each PSD and the average bulk pressure for all three PSDs after CO₂ 'huff' and 'soak', respectively. $\Delta \rho_b / \rho_b^{bef} = (\rho_b^{aft} - \rho_b^{bef}) / \rho_b^{bef}$ represents the relative increases of bulk density, where ρ_b^{aft} , ρ_b^{bef} are bulk densities of each component before and after CO₂ 'huff' and 'soak', respectively.

PSD cases	Bulk pressure P_b (bar)	$\Delta P_{b, after}$ (%)	Bulk composition				Bulk density ρ_b (kmol/m ³)				$\Delta \rho_b / \rho_b^{bef}$			
			C ₁	C ₂	C ₃	CO ₂	C ₁	C ₂	C ₃	CO ₂	C ₁	C ₂	C ₃	
Before CO ₂ 'huff' and 'soak'	EF	100	N/A	0.825	0.139	0.036	0	3.55	0.60	0.15	0	N/A	N/A	N/A
	MB	100	N/A	0.809	0.148	0.043	0	3.52	0.64	0.19	0	N/A	N/A	N/A
	HR	100	N/A	0.801	0.151	0.048	0	3.50	0.66	0.21	0	N/A	N/A	N/A
After CO ₂ 'huff' and 'soak'	EF	146.7	1.1	0.588	0.118	0.037	0.257	3.99	0.80	0.25	1.74	0.12	0.33	0.64
	MB	144.8	0.2	0.557	0.114	0.039	0.290	3.77	0.77	0.26	1.96	0.07	0.20	0.42
	HR	143.7	0.9	0.526	0.102	0.035	0.337	3.56	0.69	0.24	2.27	0.02	0.05	0.13

balance of hydrocarbon mixtures and CO₂ in the entire system during the CO₂ 'puff' process is given as,

$$\begin{cases} V_{k,b}^o(P) = \frac{m_k^o(P) - \sum_W \rho_{ave,k,W}(P) V_{p,W}}{X_{k,b}(P) \rho_b(P)} \\ m_k^{re}(P) = [V_b^o(P) - V_b] \rho_{k,b}(P) \\ m_k^n(P) = m_k^o(P) - m_k^{re}(P) \end{cases}, \quad k = C_1, C_2, C_3, CO_2 \quad (7)$$

The bulk pressure decreases by 2 bar in each step. Though P_2 in each

PSD case is slightly different as shown in Table 4, the end pressure of all PSDs is set as $P_3 = 50$ bar, which is a typical shale gas reservoir abandonment pressure [31,32,79,80].

2.3. The perturbed-chain-statistical-associating-fluid-theory-based density functional theory (PC-SAFT DFT)

The perturbed-chain-statistical-associating-fluid-theory-based density functional theory (PC-SAFT DFT) [58,59] is used to consider the chemical equilibrium between hydrocarbon fluids in bulk region and

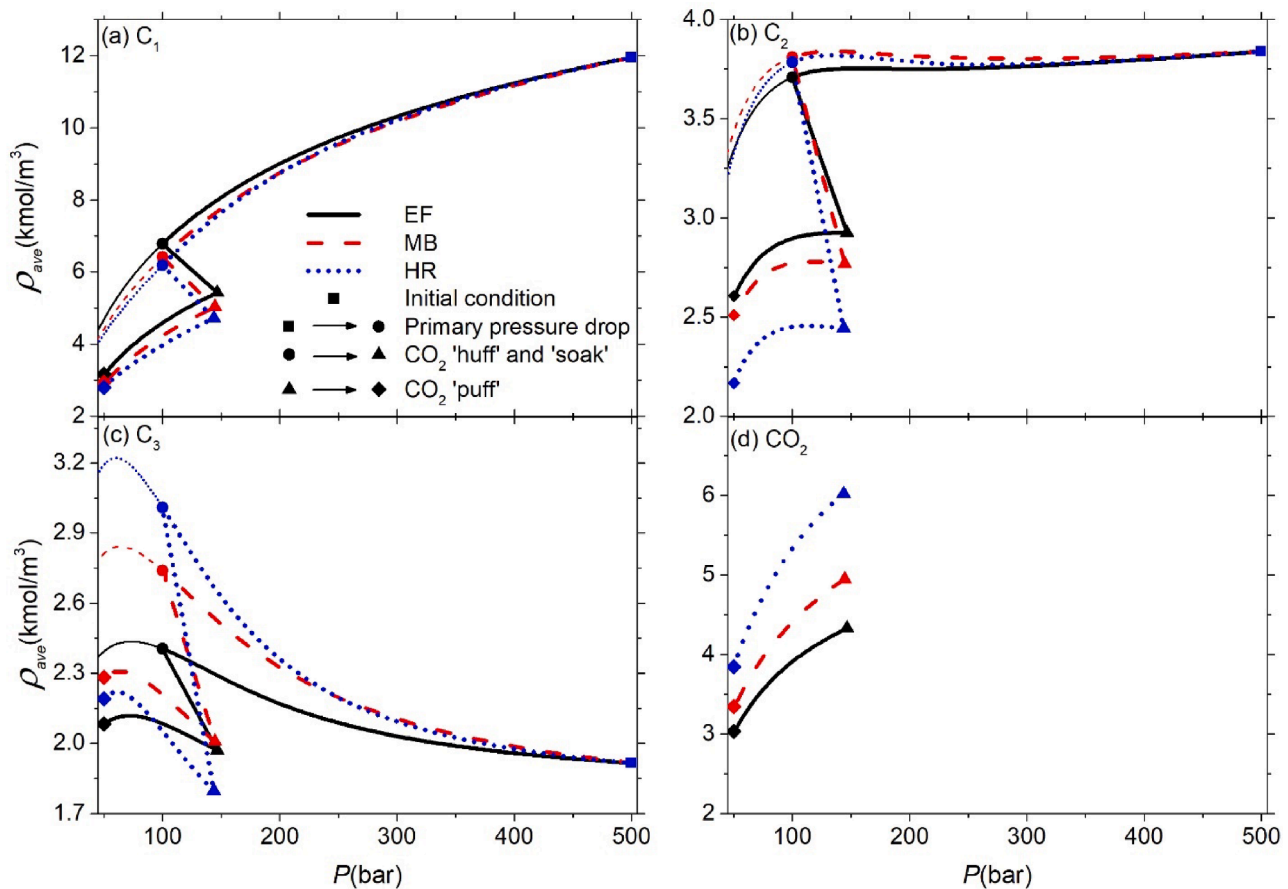


Fig. 1. The average molar densities in $W = 2$ nm pores of (a) C₁; (b) C₂; (c) C₃; and (d) CO₂ in various PSD cases at $T = 333.15$ K. The black solid lines represent average density from Eagle Ford. Red dashed lines are from Middle Bakken and blue dotted lines are from Horn River. Thick and thin lines represent CO₂ 'huff-n-puff' and direct pressure drawdown process, respectively. Squares represent the initial condition. The route from squares to circles represents the primary pressure drop; the route from circles to triangles is the CO₂ 'huff' and 'soak' processes; the route from triangles to rhombs is the CO₂ 'puff' process. (For interpretation of the references to colour in this figure legend, the reader is referred to the web version of this article.)

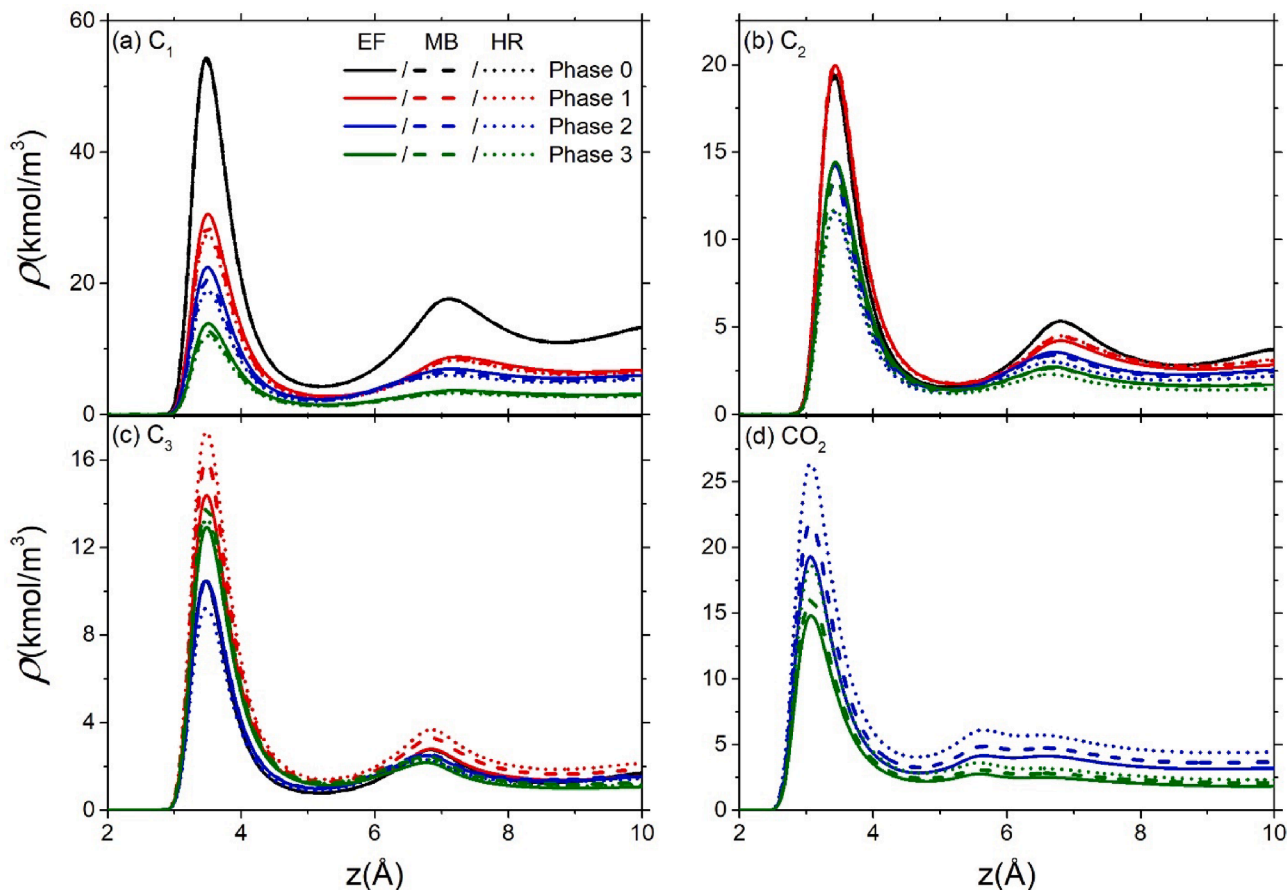


Fig. 2. The molar density profiles in $W = 2$ nm pores of (a) C_1 ; (b) C_2 ; (c) C_3 ; and (d) CO_2 in various PSD cases at $T = 333.15$ K. Black lines represent molar density profiles at initial condition (P_0). Red, bulk, and green lines represent molar density profiles at pressures of end of the primary pressure drop (P_1), CO_2 ‘huff’ and ‘soak’ (P_2), and CO_2 ‘puff’ (P_3), respectively. Solid, dashed, dotted lines represent mole density profiles from Eagle Ford, Middle Bakken, and Horn River, respectively. (For interpretation of the references to colour in this figure legend, the reader is referred to the web version of this article.)

nanopores. Based on the Wertheim’s first-order thermodynamic perturbation theory [81–84] fluid molecules in the framework of PC-SAFT DFT are treated as coarse-grained representations of real ones, where non-spherical molecules are assumed to be chains of tangentially bonded spherical segments with the Van der Waals interaction [58]. In this work, segments in each chain are treated identical [58,85]. The temperatures in nanopores and the bulk region are the same. The PC-SAFT DFT calculations are applied to the fluids in nanopores only, for a given pressure and temperature condition. The equilibrium hydrocarbon mixture and CO_2 densities in the bulk region and their density distributions in nanopores are determined by mass conservation and chemical equilibrium between the fluids in nanopores and those in bulk.

Within the framework of DFT, for a given nanopore, the grand potential $\Omega[\{\rho_k(r)\}]$, which is functional of density distribution $\{\rho_k(r)\}$, is the thermodynamic function of choice and related to the Helmholtz free-energy functional $F[\{\rho_k(r)\}]$ via the Lagrange transformation [86]

$$\Omega[\{\rho_k(r)\}] = F[\{\rho_k(r)\}] + \sum_k \int \rho_k(r) [\Psi_k(r) - \mu_k] dr, \quad (8)$$

where dr is differential volume, and $\Psi_k(r)$ is the solid surface external potential of the component k at the positional vector r ; μ_k is the chemical potential of component k in bulk [87]. $\rho_k(r)$ is the number density distribution of component k at positional vector r , given as $\rho_k(r) = m_k \rho_k^{seg}(r)$, in which m_k is the segment number of component k and $\rho_k^{seg}(r)$ is the local averaged number density of all segments of component k [58,59,66].

The Helmholtz free-energy $F[\{\rho_k(r)\}]$ is further decomposed into

two parts [59]: ideal-gas term $F^{id}[\{\rho_k(r)\}]$ and the excess term arising from the intermolecular interactions and molecular configurations $F^{ex}[\{\rho_k(r)\}]$,

$$F[\{\rho_k(r)\}] = F^{id}[\{\rho_k(r)\}] + F^{ex}[\{\rho_k(r)\}] \quad (9)$$

The ideal-gas term is given as [87]

$$\beta F^{id}[\{\rho_k(r)\}] = \sum_k \int \rho_k(r) [\ln(\rho_k(r) \Lambda_k^3) - 1] dr, \quad (10)$$

where $\beta = 1/(k_B T)$; Λ_k is the de Broglie wavelength of component k . k_B and T represent the Boltzmann constant and the absolute temperature, respectively.

In Eq. (9), molecules are modeled as chains of freely-joined spherical segments. The total excess Helmholtz free-energy $F^{ex}[\{\rho_k(r)\}]$ is given as [58,59]

$$F^{ex}[\{\rho_k(r)\}] = F^{ex,hs}[\{\rho_k(r)\}] + F^{ex,hc}[\{\rho_k(r)\}] + F^{ex,disp}[\{\rho_k(r)\}] + F^{ex,assoc}[\{\rho_k(r)\}], \quad (11)$$

where $F^{ex,hs}[\{\rho_k(r)\}]$ and $F^{ex,hc}[\{\rho_k(r)\}]$ represent the excess Helmholtz free energy arising from the hard-sphere and the connectivity of segments in hard-chain, respectively. The dispersion term $F^{ex,disp}[\{\rho_k(r)\}]$ accounts for the attractive Van der Waals interactions of chain molecules. The association term $F^{ex,assoc}[\{\rho_k(r)\}]$ describes excess Helmholtz energy due to the formation of hydrogen bonds. Details about the excess Helmholtz free-energy term $F^{ex}[\{\rho_k(r)\}]$ are shown in **Supporting Information (SI) Section 1**. In this work, the C_1 , C_2 , C_3 , and CO_2 are

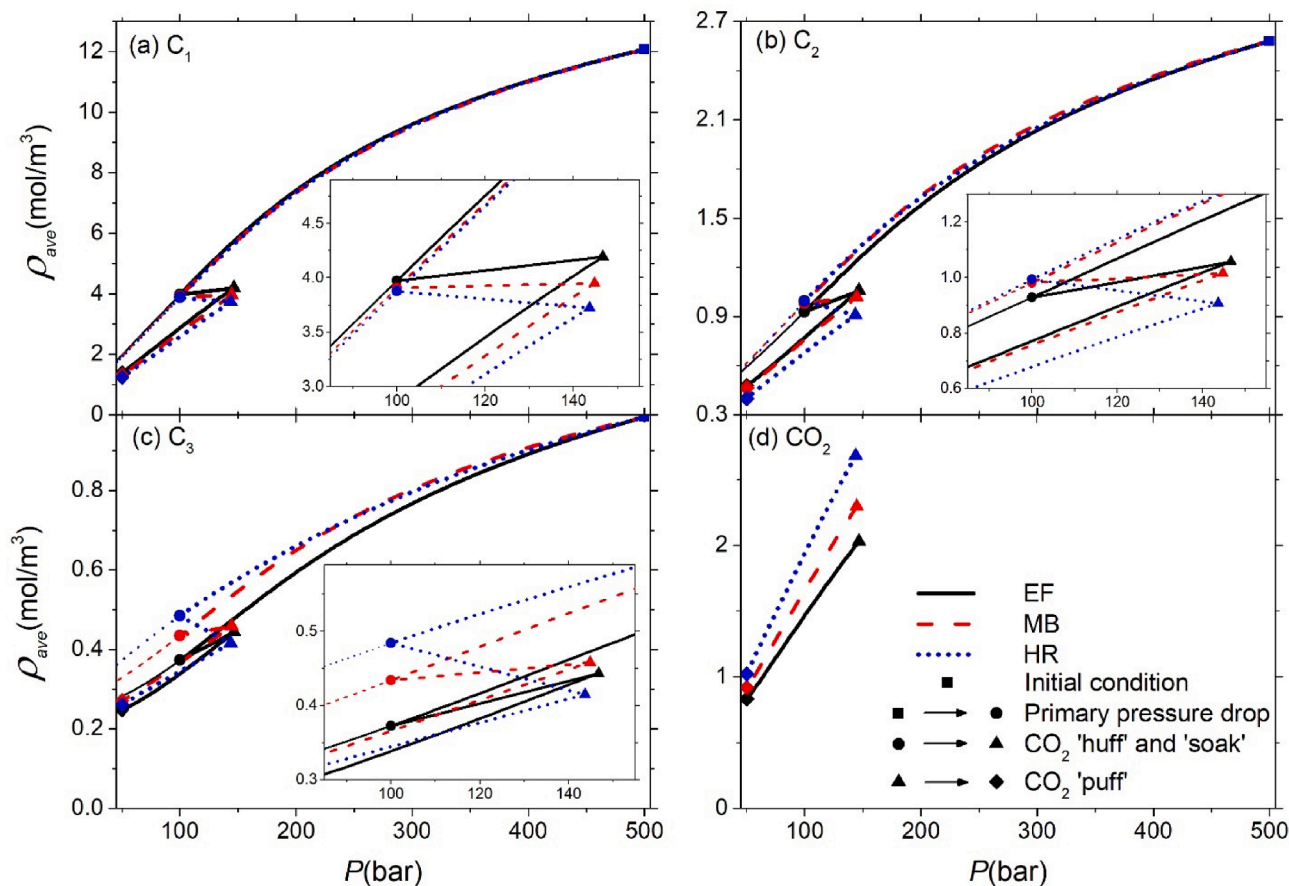


Fig. 3. The average molar densities in $W = 15$ nm pores of (a) C₁; (b) C₂; (c) C₃; and (d) CO₂ in various PSD cases at $T = 333.15$ K. The black solid lines represent average density from Eagle Ford. Red dashed lines are from Middle Bakken and blue dotted lines are from Horn River. Thick and thin lines represent scenarios with/without CO₂ 'huff-n-puff', respectively. Squares represent the initial condition. The route from squares to circles represents the primary pressure drop; the route from circles to triangles is the CO₂ 'huff' and 'soak' processes, and the route from triangles to rhombs is the CO₂ 'puff' process. The CO₂ 'huff' and 'soak' processes are amplified in inset figures. (For interpretation of the references to colour in this figure legend, the reader is referred to the web version of this article.)

considered to be without a charge so that the association term is omitted [88]. The parameters for hydrocarbons and CO₂ are from PC-SAFT EOS [89] which are listed in SI Section 2 Table S1.

At equilibrium, the grand potential functional reaches the minimum with respect to density profile $\rho_k(\mathbf{r})$ [49]

$$\frac{\delta\Omega[\{\rho_k(\mathbf{r})\}]}{\delta\rho_k(\mathbf{r})} = 0, \quad (12)$$

where the symbol δ represents the functional derivative. The equilibrium density distributions of species are obtained by the minimization of the grand potential functional [90]

$$\rho_k(\mathbf{r}) = \exp\left[\beta\mu_k - \beta\Psi_k(\mathbf{r}) - \frac{\delta\beta F^{ex}[\{\rho_k(\mathbf{r})\}]}{\delta\rho_k(\mathbf{r})}\right] \quad (13)$$

The density distribution in Eq. (13) is solved by the Picard iteration method [91]. The bulk density is used as the initialization for the calculation of the first pressure condition. The initial guess for other pressure conditions is from the density distributions at the preceding pressure [49].

For simplicity, we use carbon-slit pores which are described by two planar structureless graphite surfaces to represent nanopores in the system [42,49–51]. Such carbon nanopore structures have been applied to the study of gas adsorption in shale and shown excellent agreement with GCMC simulation results and experimental data [92]. In a carbon-slit pore, the density distributions only vary in the z direction perpendicular to the solid surfaces, *i.e.*, $\rho_k(\mathbf{r}) = \rho_k(z)$. The Steele 10-4-3 potentials [93] is used to describe the fluid-surface interactions φ_{sk} ,

$$\varphi_{sk}(z) = 2\pi m_k \rho_s \varepsilon_{sk} \sigma_{sk}^2 \Delta \left[\frac{2}{5} \left(\frac{\sigma_{sk}}{z} \right)^{10} - \left(\frac{\sigma_{sk}}{z} \right)^4 - \frac{\sigma_{sk}^4}{3\Delta(0.61\Delta + z)^3} \right], \quad (14)$$

where z represents the position in a perpendicular direction relative to the pore surface. m_k is the segment number of component k . $\rho_s = 114$ nm⁻³ is the density of graphite and $\Delta = 0.335$ nm represents the interlayer spacing of graphite; ε_{sk} and σ_{sk} are potential expansion parameters and follow the simple mixing rule: $\varepsilon_{sk} = \sqrt{\varepsilon_s \varepsilon_k}$, and $\sigma_{sk} = (\sigma_s + d_k(T))/2$. The energy and size parameters of the graphite surface are $\sigma_s = 0.3345$ nm, $\varepsilon_s/k_B = 28$ K [36,94]. ε_k is the fluid energy of segment of composition k , and $d_k(T)$ is the temperature-dependent effective segment diameter of composition k , which is defined as $d_k(T) = \sigma_k(1 - 0.12\exp(-3(\varepsilon_k/k_B T)))$ [58]. The fluid energy ε_k and the segment diameter σ_k parameters are from PC-SAFT EOS [89] and listed in SI Section 2 Table S1. In slit-nanopores, the external potential $\Psi_k(\mathbf{r})$ for component k in Eq. (13) is given as,

$$\Psi_k(z) = \varphi_{sk}(z) + \varphi_{sk}(W - z) \quad (15)$$

The average density of component k in nanopores $\rho_{ave,k}$ is calculated as,

$$\rho_{ave,k} = \frac{\int_0^{W_{ef}} \rho_k(z) dz}{W_{ef}}, \quad (16)$$

where $W_{ef} = W - \sigma_s$ is the effective pore size; W is the pore size as used in Eqs. (2) and (3) [95].

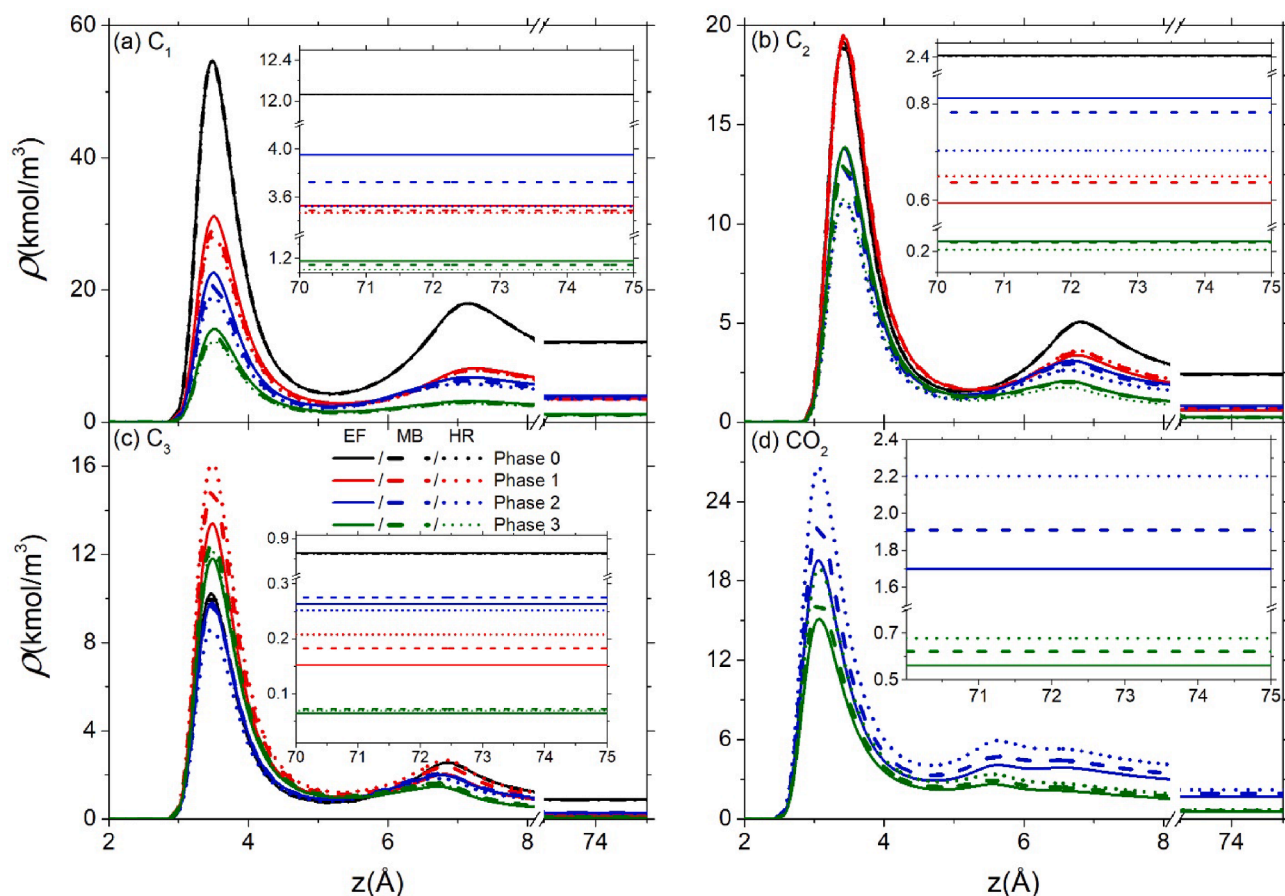


Fig. 4. The molar density profiles in $W = 15$ nm pores of (a) C_1 ; (b) C_2 ; (c) C_3 ; and (d) CO_2 in various PSD cases at $T = 333.15$ K. Black lines represent molar density profiles at initial condition (P_0). Red, bulk, and green lines represent mole density profiles at pressures of end of the primary pressure drop (P_1), CO_2 ‘huff’ and ‘soak’ (P_2), and CO_2 ‘puff’ (P_3), respectively. Solid, dashed, dotted lines represent mole density profiles from Eagle Ford, Middle Bakken, and Horn River, respectively. The densities of the middle of pores are amplified shown as inserted figures. (For interpretation of the references to colour in this figure legend, the reader is referred to the web version of this article.)

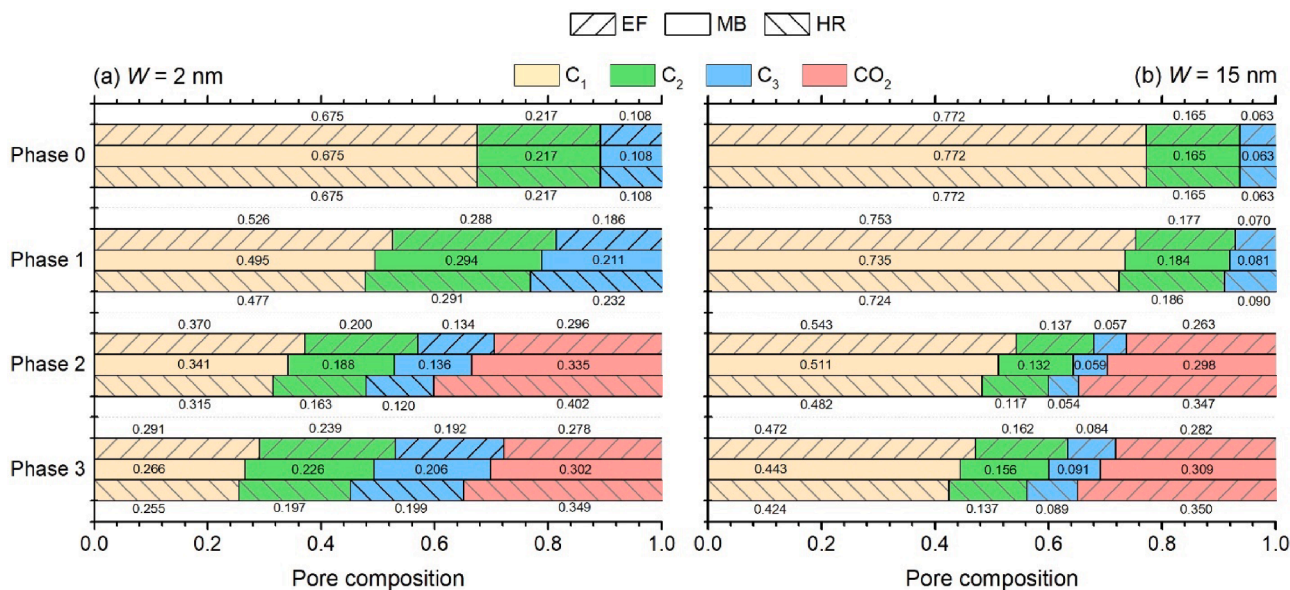


Fig. 5. Compositions of each component in (a) $W = 2$ nm; (b) $W = 15$ nm pores in various PSD cases at $T = 333.15$ K. Phase 0 represents the initial condition; Phase 1 represents the primary pressure drop process; Phase 2 is the CO_2 ‘huff’ and ‘soak’ process, and Phase 3 is the CO_2 ‘puff’ process. The pore compositions shown for Phase 1, 2, 3 are the composition at the pressure of the end of each phase.

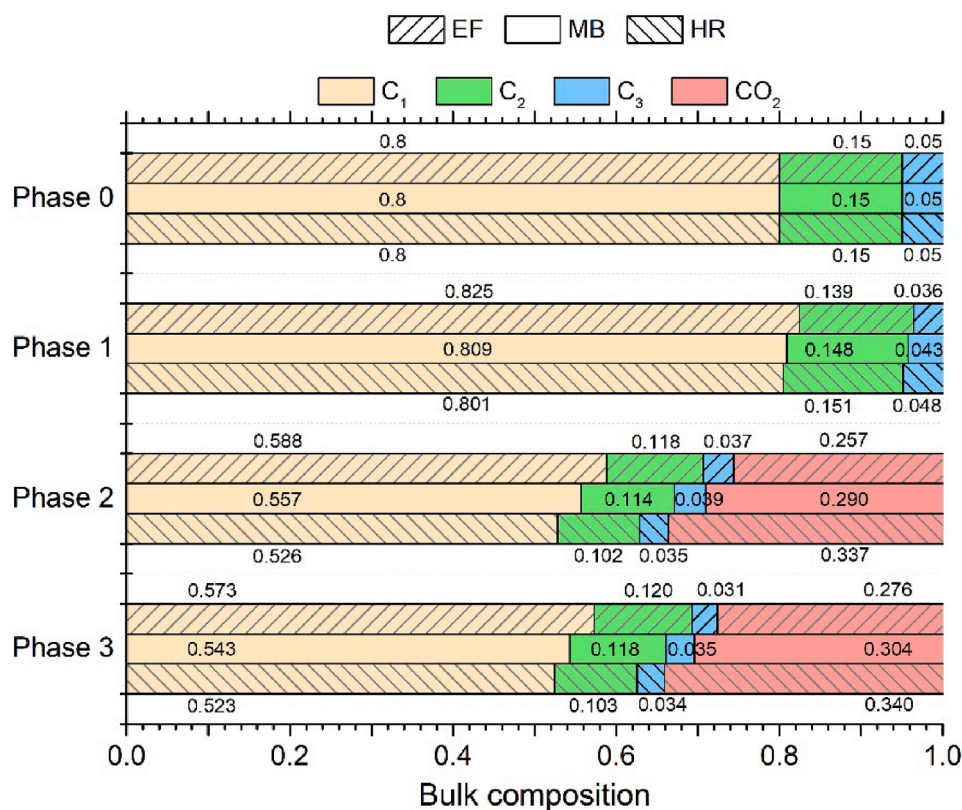


Fig. 6. Bulk compositions of each component in various PSD cases. Phase 0 represents the initial condition at $T = 333.15$ K; Phase 1 represents the primary pressure drop process; Phase 2 is the CO₂ ‘huff’ and ‘soak’ process, and Phase 3 is the CO₂ ‘puff’ process. The bulk compositions shown for Phase 1, 2, 3 are the composition at the pressure of the end of each phase.

2.4. Grand canonical monte carlo (GCMC) simulation

GCMC simulation has been widely used as one of the most powerful tools to study hydrocarbons and CO₂ adsorption under confinement [26,96–99]. To calibrate our PC-SAFT DFT calculations, we compared density profiles and average densities in nanopores of hydrocarbon and CO₂ mixtures from PC-SAFT DFT with those from GCMC simulations. The details of GCMC simulation and comparison with PC-SAFT DFT are shown in SI Section 3, and SI Section 4, respectively.

3. Results and discussions

In this section, we use three simplified PSDs from Eagle Ford (EF) [71] Middle Bakken (MB) [73] and Horn River (HR) [72] shale subformations to study the effect of volume partitioning on hydrocarbons and CO₂ mixture adsorption during CO₂ ‘huff-n-puff’ process. The initial mole fractions in the bulk region are set the same in each PSD case as shown in Table 2.

In Fig. 1, we present the average molar densities of hydrocarbons and CO₂ during CO₂ ‘huff-n-puff’ process in $W = 2$ nm pores. For comparison, we also depict the average molar densities in a direct pressure drawdown from P_0 to P_3 . During the primary pressure drawdown from P_0 to P_1 , C₁ is released from the pores, while C₃ adsorption in micropores increases. As P drops, the PSD case with a higher volume ratio of smaller pores (i.e. EF) releases less C₁ and C₂ from 2-nm pores, while adsorbing less C₃. As CO₂ is injected, the bulk pressure increases with slight differences among three PSD cases as shown in Table 4. During the CO₂ ‘huff’ and ‘soak’ process, the decrease in all hydrocarbon densities is smaller in the EF case. In addition, with the same amount of injected CO₂, the CO₂ average density in the 2-nm pores in the EF case is the lowest. During the CO₂ ‘puff’ process, C₁ is continuously released from pores, while C₃ adsorption in micropores increases, then decreases at

low pressures. The CO₂ average density decreases in all PSD cases during the CO₂ ‘puff’ process, while CO₂ adsorption in the EF case decreases less.

In Fig. 2, we present molar density profiles of hydrocarbons and CO₂ in 2-nm pores. During the primary pressure drawdown, C₁ densities in the adsorption layer and the middle of the pores decrease, while the opposite is true for C₃ due to strong fluid-surface interactions, as in our previous work [37]. During the CO₂ ‘huff’ and ‘soak’ process, C₁, C₂, and C₃ are released from both adsorption layers and the middle of pores. In the EF case, hydrocarbon release from the 2-nm pores due to the CO₂ ‘huff’ and ‘soak’ is less significant than those in the MB and HR cases, especially for C₃. Due to the stronger competitive adsorption in the vicinity of the pore surface, the volume partitioning shows a more obvious effect on adsorption layers. On the other hand, due to volume partitioning and competitive adsorption between CO₂ and hydrocarbon mixtures, CO₂ densities in the adsorption layers and the middle of the pores in the EF case is the smallest in all PSD cases. In this work, during the CO₂ ‘huff’ and ‘soak’ process, the same amount of CO₂ is injected into different PSD cases. Due to the highest micropore volume in EF, the total amount of adsorbed CO₂ in micropores is the highest, which in turn results in the lowest CO₂ composition in the bulk region. Thanks to the chemical equilibrium, the CO₂ density of CO₂ in micropores in the EF case is the lowest. During the CO₂ ‘puff’ process, C₁, C₂, and CO₂ densities decrease, while C₃ density increases. Compared with other PSD cases, the EF case releases more C₁, C₂, and CO₂, while adsorbs less C₃, which is opposite to that during the primary pressure drop.

The average molar densities of each component in $W = 15$ nm pores are shown in Fig. 3. The average densities for $W = 5$ nm and $W = 30$ nm pores as well as in the bulk region are shown in SI Section 5. During the primary pressure drop, all hydrocarbon densities decrease as P drops. During the CO₂ ‘huff’ and ‘soak’ processes, hydrocarbon densities increase in the EF and MB cases as CO₂ is injected, while the opposite is

true for the HR case. For CO₂, similar to Fig. 1, its average molar density in the EF case is higher. During the CO₂ ‘puff’ process, all components are released from the pores as pressure drops.

In Fig. 4, we present the molar density profiles for each component in $W = 15$ nm pores. The molar density profiles for $W = 5$ nm and $W = 30$ nm pores are shown in SI Section 6. During the primary pressure drop, C₁ is released from adsorption layers and the middle of pores, while C₂ and C₃ are mostly released from the middle of pores. The change in the C₂ adsorption layers is negligible, while the C₃ adsorption layer becomes more prominent. The CO₂ ‘huff’ and ‘soak’ process has an opposite effect on hydrocarbons densities in the adsorption layers and the middle of pores: they are released from adsorption layers, while their densities in the middle of pores increase.

The effect of volume partitioning on the compositions of each component in $W = 2$ nm and $W = 15$ nm is shown in Fig. 5. The compositions of each component in $W = 5$ nm and $W = 30$ nm pores are shown in SI Section 7. During the CO₂ ‘huff’ and ‘soak’ process, PSD strongly affects the equilibrium compositions in micro-/mesopores. In the EF case, the compositions of hydrocarbons in pores reduce less. During the CO₂ ‘puff’ process, in $W = 2$ nm pores, though C₁, C₂, and CO₂ are released from pores, the C₁ and CO₂ compositions decrease, while the C₂ composition increases. On the other hand, the C₃ composition in 2-nm pores increases. In $W = 15$ nm pores, C₁ composition decreases, while C₂ and C₃ compositions increase. However, the CO₂ composition increases in $W = 15$ nm pores.

The bulk pressure, composition, and densities of hydrocarbon components and CO₂ in various PSD cases before and after CO₂ ‘huff’ and ‘soak’ processes are listed in Table 4. Though the same amount of CO₂ is injected in each PSD case, more CO₂ is adsorbed into micro-/mesopores in the EF case. Thus, in the EF case, the CO₂ equilibrium bulk composition is smaller, while the hydrocarbon component compositions are higher. On the other hand, P_2 in different PSD cases are similar. Meanwhile, the bulk density increases due to CO₂ injection, while increasing more in the EF case. Bulk compositions in different PSD cases are also presented in Fig. 6. During the CO₂ ‘huff’ and ‘soak’ process, PSD strongly affects the equilibrium bulk compositions. As the volume ratio of the bulk region decreases, more CO₂ is absorbed into micro-/mesopores, and more hydrocarbons (C₁, C₂, and C₃) are released from the micro-/mesopores to the bulk region. As a result, in the EF case, the hydrocarbon bulk composition is higher. In turn, their average molar densities in micro-/mesopores increase. During the CO₂ ‘puff’ process, both C₂ and CO₂ bulk compositions increase as P drops, while the opposite is true for C₁ and C₃.

To investigate hydrocarbons recovery from nanopores and the bulk region in different phases, we calculate the hydrocarbon-releasing factor, which is given as,

$$\text{Hydrocarbon-releasing factor} = \frac{\rho_k^{beg} - \rho_k^{end}}{\rho_k^{int}}, \quad k = C_1, C_2, C_3, \quad (17)$$

where ρ_k^{beg} , ρ_k^{end} represent bulk or pore molar density of component k at the beginning and end of a phase, respectively. ρ_k^{int} represents bulk or pore molar density of component k at the initial condition (i.e. Phase 0). In Fig. 7, we present hydrocarbon-releasing factors in nanopores ($W = 2$ nm and $W = 15$ nm) and the bulk region in various PSD cases. The hydrocarbon-releasing factors in $W = 5$ nm and $W = 30$ nm pores are shown in SI Section 8. During the primary pressure drop, the EF case has a lower C₁-releasing factor, while higher C₂- and C₃-releasing factors in both pores and the bulk region. During the CO₂ ‘huff’ and ‘soak’ process, the EF case has a lower releasing factor for all components in both pores and the bulk region. The recovery of hydrocarbon mixtures for the CO₂ ‘huff’ and ‘soak’ process is mainly from small pores. In the CO₂ ‘puff’ process, the EF case has higher releasing factors for all components in pores and higher C₁- and C₂-releasing factors in the bulk, while the MB shows a slightly higher C₃-releasing factor in the bulk.

In Fig. 8, hydrocarbon components recoveries from the entire

nanopore-bulk multiscale system in different phases and various PSD cases with CO₂ ‘huff-n-puff’ process are shown, which is defined as,

$$\text{Recovery} = \frac{N_k^{beg} - N_k^{end}}{N_k^{int}}, \quad k = C_1, C_2, C_3, \quad (18)$$

where N_k^{beg} and N_k^{end} represent the molar number of component k at the beginning and end of each phase, respectively. N_k^{int} represents the molar number of component k at the initial condition. As there is no production during the CO₂ ‘huff’ and ‘soak’ process, the recovery is zero in Phase 2. To show the CO₂ ‘huff-n-puff’ enhancement effect, hydrocarbon recovery in each pore, the bulk region as well as the entire nanopore-bulk multiscale system with/without CO₂ ‘huff-n-puff’ processes are listed in Table 5. The CO₂ ‘huff-n-puff’ process enhances the total hydrocarbon

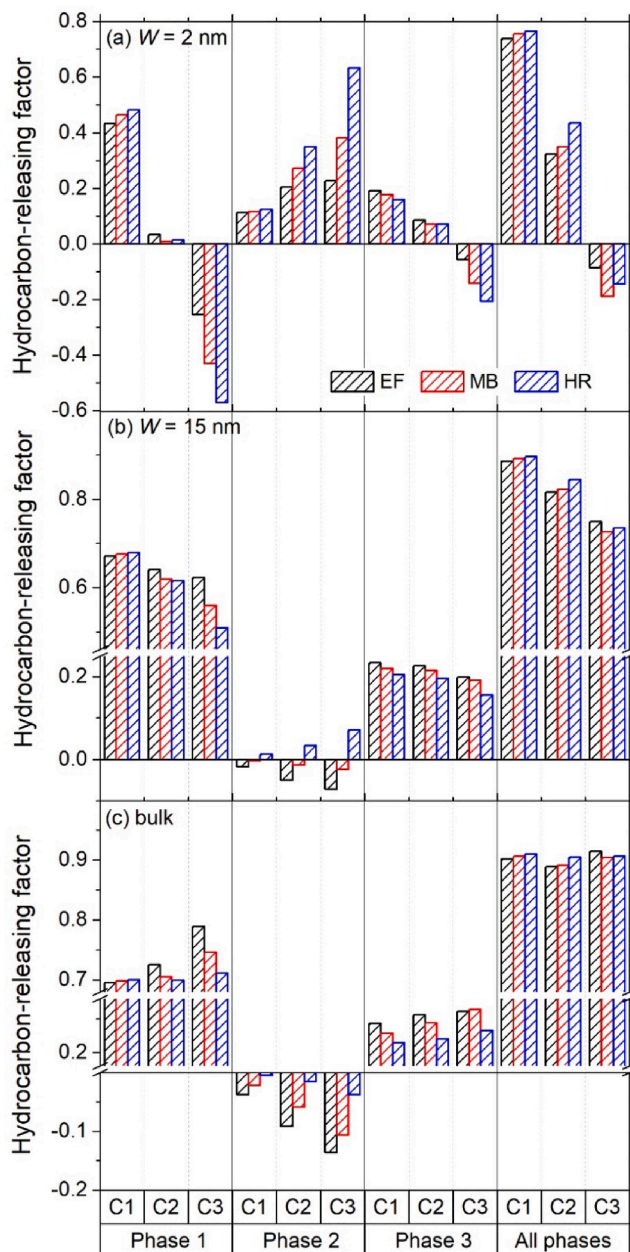


Fig. 7. The hydrocarbon-releasing factors in (a) $W = 2$ nm; (b) $W = 15$ nm; (c) the bulk region in various PSD cases at $T = 333.15$ K. Phase 1 represents the primary pressure drop process; Phase 2 is the CO₂ ‘huff’ and ‘soak’ process, and Phase 3 is the CO₂ ‘puff’ process; All phases represent the whole process from the initial condition to the abandoned pressure in the CO₂ ‘huff-n-puff’.

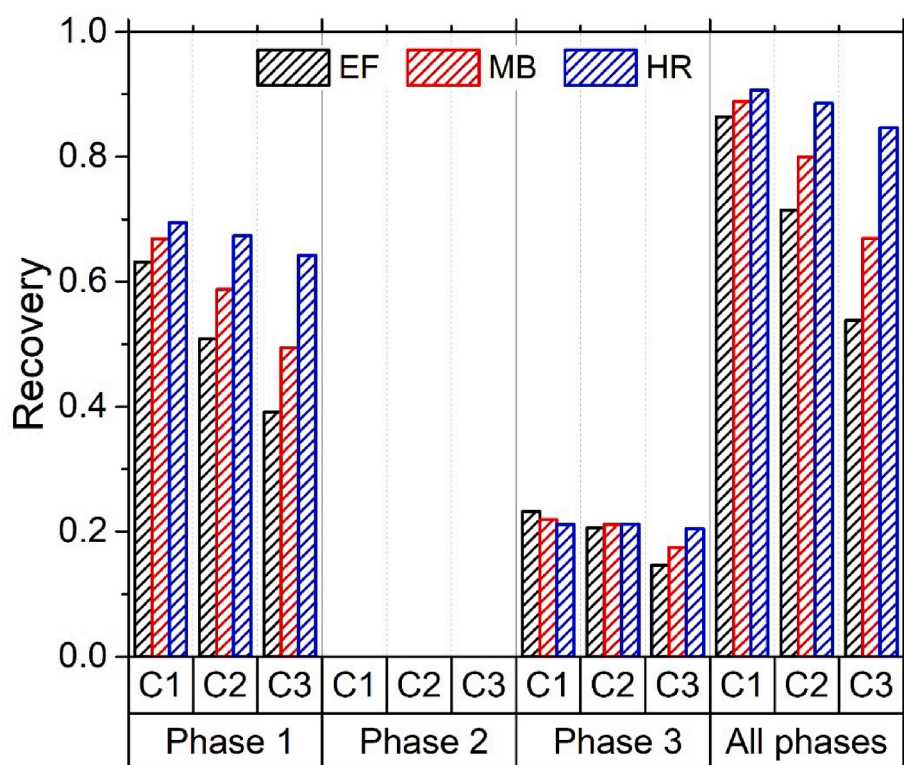


Fig. 8. The recovery of hydrocarbon components in the nanopore-bulk multiscale system in different phases in various PSD cases with CO₂ 'huff-n-puff' process at $T = 333.15$ K. Phase 1 represents the primary pressure drop process; Phase 2 is the CO₂ 'huff' and 'soak' process, and Phase 3 is the CO₂ 'puff' process; All phases represent the whole process from the initial condition to the abandoned pressure in the CO₂ 'huff-n-puff'.

Table 5

Hydrocarbon recoveries in each pore, the bulk region, and the entire nanopore-bulk multiscale system with/without the CO₂ 'huff-n-puff' process. Note that w/ and w/o represent with and without, respectively.

PSD cases	Recovery																		
	2nm			5nm			15nm			30nm			Bulk			System			
	C ₁	C ₂	C ₃	C ₁	C ₂	C ₃	C ₁	C ₂	C ₃	C ₁	C ₂	C ₃	C ₁	C ₂	C ₃	C ₁	C ₂	C ₃	
W/ CO ₂ injection	EF	0.737	0.323	-0.085	0.847	0.671	0.485	0.887	0.816	0.749	0.896	0.857	0.833	0.902	0.889	0.915	0.864	0.715	0.538
	MB	0.756	0.349	-0.189	0.856	0.684	0.440	0.893	0.822	0.726	0.901	0.860	0.817	0.906	0.891	0.904	0.888	0.799	0.669
	HR	0.765	0.434	-0.144	0.861	0.724	0.459	0.897	0.844	0.735	0.905	0.878	0.822	0.910	0.904	0.906	0.906	0.886	0.846
W/O CO ₂ injection	EF	0.608	0.129	-0.249	0.776	0.580	0.402	0.837	0.771	0.715	0.851	0.824	0.814	0.861	0.867	0.910	0.802	0.639	0.469
	MB	0.630	0.105	-0.468	0.783	0.569	0.308	0.841	0.762	0.667	0.854	0.816	0.780	0.863	0.859	0.889	0.834	0.731	0.596
	HR	0.641	0.134	-0.667	0.786	0.583	0.221	0.842	0.768	0.622	0.855	0.820	0.749	0.863	0.860	0.871	0.857	0.831	0.784
Enhanced Recovery	EF	12.9%	19.3%	16.4%	7.1%	9.1%	8.3%	5.0%	4.5%	3.5%	4.5%	3.3%	2.0%	4.1%	2.2%	0.5%	6.2%	7.6%	6.9%
	MB	12.6%	24.4%	27.9%	7.3%	11.5%	13.2%	5.2%	6.0%	5.9%	4.7%	4.4%	3.6%	4.4%	3.2%	1.5%	5.4%	6.9%	7.3%
	HR	12.3%	30.0%	52.3%	7.5%	14.1%	23.8%	5.5%	7.6%	11.2%	5.0%	5.8%	7.3%	4.6%	4.4%	3.5%	4.9%	5.4%	6.2%

recovery by more than 5%, while the enhancement in the heavier component recovery in small pores (2-nm pores) can be between 16.4% and 52.3% in different PSD cases. Due to the volume partitioning, the EF case has the highest enhanced hydrocarbon recovery due to the CO₂ 'huff-n-puff' process.

The CO₂ sequestration ratio in nanopores, bulk, and the total nanopore-bulk multiscale system in various PSD cases are shown in Fig. 9, which is defined as,

$$\text{CO}_2 \text{ sequestration ratio} = \frac{N_{\text{CO}_2}^{\text{sequestered}}}{N_{\text{CO}_2}^{\text{after_soak}}} \quad (19)$$

where $N_{\text{CO}_2}^{\text{sequestered}}$ represents the molar number of CO₂ remaining in nanopores, bulk, or the total nanopore-bulk multiscale system at the abandoned pressure, and $N_{\text{CO}_2}^{\text{after_soak}}$ represents the initial molar number of CO₂ in nanopores, bulk, or the total nanopore-bulk multiscale system after CO₂ 'huff' and 'soak' process. A stronger confinement effect in smaller pores allows enhancing CO₂ storage. A higher volume ratio of smaller pores case can store more CO₂ in nanopores and the bulk region.

As a result, the PSD with a higher volume ratio of smaller pores has a higher total CO₂ sequestration ratio.

4. Conclusions

In this work, we use the PC-SAFT DFT to study the CO₂ 'huff-n-puff' process in a nanopore-bulk multiscale system by a CVD process, in which mass balance and volume partitioning are explicitly considered. During the CO₂ 'huff' and 'soak' process, a large amount of hydrocarbons can be released from small micro-/mesopores, especially for the heavier components. On the other hand, in the larger mesopores ($W \geq 15$ nm), the average density of hydrocarbons might increase. For hydrocarbon density distributions, the CO₂ injection has mixed influences on the adsorption layers and the middle of pores: hydrocarbons are released from the adsorption layers, while their densities in the middle of pores increase. Compared with the case without the CO₂ 'huff-n-puff' process, the CO₂ 'huff-n-puff' process prompts hydrocarbon release from nanopores, especially for the heavier components in the smaller micro-/mesopores.

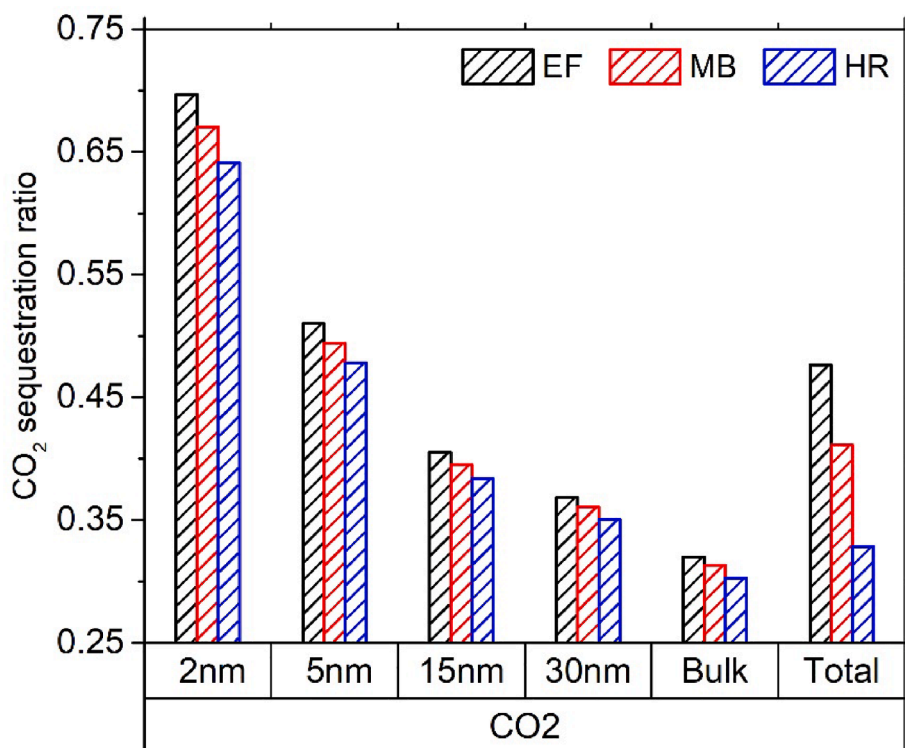


Fig. 9. The CO₂ sequestration ratio in nanopores, bulk, and the total nanopore-bulk multiscale system in various PSDs.

The volume partitioning effects on nanopores adsorption, compositions are significant in the CO₂ 'huff-n-puff' process. During the CO₂ 'huff' and 'soak' process, a PSD case with a higher volume ratio of smaller pores ($W = 2$ nm and $W = 5$ nm) releases fewer hydrocarbons (C₁, C₂, C₃). The volume partitioning also shows a more obvious effect on altering the density of adsorption layers than that in the middle of pores, especially in the larger pores ($W \geq 15$ nm). In addition, it also shows a strong influence on the equilibrium bulk composition. Hydrocarbon recovery is also strongly affected by volume partitioning. For small micro-/mesopores ($W = 2$ nm and $W = 5$ nm), the recovery of C₂ and C₃ mainly stems from the CO₂ 'huff' and 'soak' period, while, in larger pores ($W \geq 15$ nm), the hydrocarbon recovery is mainly from pressure drops. In the nanopore-bulk multiscale system, the hydrocarbon recovery due to CO₂ injection is mainly from the smaller pores ($W = 2$ nm and $W = 5$ nm). The smaller micro-/mesopores with a stronger confinement effect can adsorb more CO₂ per unit pore volume. As a result, a PSD case with a higher volume ratio of smaller pores can store more CO₂.

Collectively, the volume partitioning shows strong influences in hydrocarbon adsorption and recovery as well as CO₂ sequestration in nanopores during CO₂ 'huff-n-puff' process. Our work should provide fundamental understandings about the effect of volume partitioning on hydrocarbon mixtures adsorption characteristics and important insights into the optimization of enhanced shale gas recovery and CO₂ sequestration. On the other hand, moisture exists in shale media which can affect hydrocarbon and CO₂ adsorption [13]. Besides, kerogen in shale can contain various heteroatoms [30,47,100]. Unlocking these effects coupled with volume partitioning in the nanopore-bulk multiscale system on hydrocarbon and CO₂ adsorption will be explicitly studied in our future works.

Declaration of Competing Interest

The authors declare that they have no known competing financial interests or personal relationships that could have appeared to influence the work reported in this paper.

Acknowledgments

This research is partly supported by Westgrid (www.westgrid.ca) and Compute Canada (www.computecanada.ca). The authors also acknowledge a Discovery Grant from the Natural Sciences and Engineering Research Council of Canada (NSERC RGPIN-2017-05080). As a part of the University of Alberta's Future Energy Systems research initiative, this research was made possible in part thanks to funding from the Canada First Research Excellence Fund.

References

- [1] M. Gasparik, A. Ghanizadeh, P. Bertier, Y. Gensterblum, S. Bouw, B. Krooss, High-pressure methane sorption isotherms of black shales from The Netherlands, *Energy Fuels* 26 (2012) 4995–5004.
- [2] IEA (2019), World Energy Outlook 2019, IEA, Paris <https://www.iea.org/reports/world-energy-outlook-2019>.
- [3] G.R. Chalmers, R.M. Bustin, I.M. Power, Characterization of gas shale pore systems by porosimetry, pycnometry, surface area, and field emission scanning electron microscopy/transmission electron microscopy image analyses: examples from the Barnett, Woodford, Haynesville, Marcellus, and Doig units, *AAPG Bull.* 96 (2012) 1099–1119.
- [4] N.S. Alharthy, T. Nguyen, T. Teklu, H. Kazemi, R. Graves, Multiphase compositional modeling in small-scale pores of unconventional shale reservoirs, in: *SPE Annual Technical Conference and Exhibition*, Society of Petroleum Engineers, New Orleans, Louisiana, USA, 2013, p. 20.
- [5] O. Arogundade, M. Sohrabi, A Review of Recent Developments and Challenges in Shale Gas Recovery, *SPE Saudi Arabia Section Technical Symposium and Exhibition*, Society of Petroleum Engineers, Al-Khobar, Saudi Arabia, 2012, pp. 31.
- [6] L. Jin, Y. Ma, A. Jamili, Investigating the effect of pore proximity on phase behavior and fluid properties in shale formations, in: *SPE Annual Technical Conference and Exhibition*, Society of Petroleum Engineers, New Orleans, Louisiana, USA, 2013, p. 16.
- [7] P. Psarras, R. Holmes, V. Vishal, J. Wilcox, Methane and CO₂ adsorption capacities of kerogen in the eagle ford shale from molecular simulation, *Acc. Chem. Res.* 50 (2017) 1818–1828.
- [8] K. Louk, N. Ripepi, K. Luxbacher, E. Gilliland, X. Tang, C. Keles, C. Schlosser, E. Diminick, S. Keim, J. Amante, K. Michael, Monitoring CO₂ storage and enhanced gas recovery in unconventional shale reservoirs: results from the Morgan County, Tennessee injection test, *J. Nat. Gas Sci. Eng.* 45 (2017) 11–25.
- [9] R. Sandrea, Evaluating production potential of mature US oil, gas shale plays, *Oil Gas J.* 110 (2012) 58–67.

- [10] Z. Li, M. Dong, S. Li, S. Huang, CO₂ sequestration in depleted oil and gas reservoirs—caprock characterization and storage capacity, *Energy Convers. Manage.* 47 (2006) 1372–1382.
- [11] R. Shukla, P. Ranjith, A. Haque, X. Choi, A review of studies on CO₂ sequestration and caprock integrity, *Fuel* 89 (2010) 2651–2664.
- [12] M. Bui, C.S. Adjiman, A. Bardow, E.J. Anthony, A. Boston, S. Brown, P.S. Fennell, S. Fuss, A. Galindo, L.A. Hackett, J.P. Hallett, H.J. Herzog, G. Jackson, J. Kemper, S. Krevor, G.C. Maitland, M. Matuszewski, I.S. Metcalfe, C. Petit, G. Puxty, J. Reimer, D.M. Reiner, E.S. Rubin, S.A. Scott, N. Shah, B. Smit, J.P.M. Trusler, P. Webley, J. Wilcox, N. Mac Dowell, Carbon capture and storage (CCS): the way forward, *Energy Environ. Sci.* 11 (2018) 1062–1176.
- [13] J. Zhou, Z. Jin, K.H. Luo, The role of brine in gas adsorption and dissolution in kerogen nanopores for enhanced gas recovery and CO₂ sequestration, *Chem. Eng. J.* 399 (2020), 125704.
- [14] R. Iddphonce, J. Wang, L. Zhao, Review of CO₂ injection techniques for enhanced shale gas recovery: prospect and challenges, *J. Nat. Gas Sci. Eng.* 77 (2020), 103240.
- [15] E. Mohagheghian, H. Hassanzadeh, Z. Chen, CO₂ sequestration coupled with enhanced gas recovery in shale gas reservoirs, *J. CO₂ Util.* 34 (2019) 646–655.
- [16] D.S. Berawala, P. Østebø Andersen, Evaluation of multicomponent adsorption kinetics for CO₂ enhanced gas recovery from tight shales, in: *SPE Europe* featured at 81st EAGE Conference and Exhibition, Society of Petroleum Engineers, London, England, UK, 2019, p. 26.
- [17] M.O. Eshkalak, E.W. Al-shalabi, A. Sanaei, U. Aybar, K. Sepehrmoori, Enhanced gas recovery by CO₂ sequestration versus re-fracturing treatment in unconventional shale gas reservoirs, in: *Abu Dhabi International Petroleum Exhibition and Conference*, Society of Petroleum Engineers, Abu Dhabi, UAE, 2014, p. 18.
- [18] J.J. Sheng, Critical review of field EOR projects in shale and tight reservoirs, *J. Petrol. Sci. Eng.* 159 (2017) 654–665.
- [19] R. Holmes, H. Aljamaan, V. Vishal, J. Wilcox, A.R. Kovscek, Idealized shale sorption isotherm measurements to determine pore capacity, pore size distribution, and surface area, *Energy Fuels* 33 (2019) 665–676.
- [20] J. Liu, Y. Yao, D. Liu, D. Elsworth, Experimental evaluation of CO₂ enhanced recovery of adsorbed-gas from shale, *Int. J. Coal Geol.* 179 (2017) 211–218.
- [21] J. Liu, L. Xie, Y. Yao, Q. Gan, P. Zhao, L. Du, Preliminary study of influence factors and estimation model of the enhanced gas recovery stimulated by carbon dioxide utilization in shale, *ACS Sustain. Chem. Eng.* 7 (2019) 20114–20125.
- [22] L. Li, C. Li, T. Kang, Adsorption/desorption behavior of CH₄ on shale during the CO₂ huff-and-puff process, *Energy Fuels* 33 (2019) 5147–5152.
- [23] R. Xu, K. Zeng, C. Zhang, P. Jiang, Assessing the feasibility and CO₂ storage capacity of CO₂ enhanced shale gas recovery using Triple-Porosity reservoir model, *Appl. Therm. Eng.* 115 (2017) 1306–1314.
- [24] T.H. Kim, J. Cho, K.S. Lee, Evaluation of CO₂ injection in shale gas reservoirs with multi-component transport and geomechanical effects, *Appl. Energy* 190 (2017) 1195–1206.
- [25] M. Wu, M. Ding, J. Yao, C. Li, X. Li, J. Zhu, Development of a multi-continuum quadruple porosity model to estimate CO₂ storage capacity and CO₂ enhanced shale gas recovery, *J. Petrol. Sci. Eng.* 178 (2019) 964–974.
- [26] H. Sui, J. Yao, Effect of surface chemistry for CH₄/CO₂ adsorption in kerogen: a molecular simulation study, *J. Nat. Gas Sci. Eng.* 31 (2016) 738–746.
- [27] Q. Yuan, X. Zhu, K. Lin, Y.-P. Zhao, Molecular dynamics simulations of the enhanced recovery of confined methane with carbon dioxide, *PCCP* 17 (2015) 31887–31893.
- [28] K. Zeng, P. Jiang, Z. Lun, R. Xu, Molecular simulation of carbon dioxide and methane adsorption in shale organic nanopores, *Energy Fuels* 33 (2019) 1785–1796.
- [29] L. Huang, Z. Ning, Q. Wang, R. Qi, Y. Zeng, H. Qin, H. Ye, W. Zhang, Molecular simulation of adsorption behaviors of methane, carbon dioxide and their mixtures on kerogen: effect of kerogen maturity and moisture content, *Fuel* 211 (2018) 159–172.
- [30] J. Zhou, Z. Jin, K.H. Luo, Effects of moisture contents on shale gas recovery and CO₂ sequestration, *Langmuir* 35 (2019) 8716–8725.
- [31] J. Zhou, Z. Jin, K.H. Luo, Insights into recovery of multi-component shale gas by CO₂ injection: a molecular perspective, *Fuel* 267 (2020), 117247.
- [32] M. Zhang, S. Zhan, Z. Jin, Recovery mechanisms of hydrocarbon mixtures in organic and inorganic nanopores during pressure drawdown and CO₂ injection from molecular perspectives, *Chem. Eng. J.* 382 (2020), 122808.
- [33] S. Bakhshian, S.A. Hosseini, Prediction of CO₂ adsorption-induced deformation in shale nanopores, *Fuel* 241 (2019) 767–776.
- [34] L. T. R. Ko, Origin and characterization of Eagle Ford pore networks in the south Texas Upper Cretaceous shelf, *AAPG Bulletin* 101 (2017) 387–418.
- [35] D.J.K. Ross, R. Marc Bustin, The importance of shale composition and pore structure upon gas storage potential of shale gas reservoirs, *Mar. Pet. Geol.* 26 (2009) 916–927.
- [36] Y. Zhao, Z. Jin, Hydrocarbon-phase behaviors in shale nanopore/fracture model: multiscale, multicomponent, and multiphase, *SPE J.* 24 (2019) 2526–2540.
- [37] Y. Wang, Z. Jin, Effect of pore size distribution on hydrocarbon mixtures adsorption in shale nanoporous media from engineering density functional theory, *Fuel* 254 (2019), 115650.
- [38] S. Luo, J.L. Lutkenhaus, H. Nasrabadi, Effect of nanoscale pore-size distribution on fluid phase behavior of gas-improved oil recovery in shale reservoirs, *SPE J.* 25 (2020) 1406–1415.
- [39] B. Jin, R. Bi, H. Nasrabadi, Molecular simulation of the pore size distribution effect on phase behavior of methane confined in nanopores, *Fluid Phase Equilib.* 452 (2017) 94–102.
- [40] L. Wang, X. Yin, K.B. Neeves, E. Ozkan, Effect of pore-size distribution on phase transition of hydrocarbon mixtures in nanoporous media, *SPE J.* 21 (2016) 1981–1995.
- [41] J. Zhong, Y. Zhao, C. Lu, Y. Xu, Z. Jin, F. Mostowfi, D. Sinton, Nanoscale phase measurement for the shale challenge: multicomponent fluids in multiscale volumes, *Langmuir* 34 (2018) 9927–9935.
- [42] Y. Zhao, Y. Wang, J. Zhong, Y. Xu, D. Sinton, Z. Jin, Bubble point pressures of hydrocarbon mixtures in multiscale volumes from density functional theory, *Langmuir* 34 (2018) 14058–14068.
- [43] S. Luo, J.L. Lutkenhaus, H. Nasrabadi, Multi-scale fluid phase behavior simulation in shale reservoirs by a pore-size-dependent equation of state, in: *SPE Annual Technical Conference and Exhibition*, Society of Petroleum Engineers, San Antonio, Texas, USA, 2017, p. 22.
- [44] S. Luo, J.L. Lutkenhaus, H. Nasrabadi, Experimental study of pore size distribution effect on phase transitions of hydrocarbons in nanoporous media, *Fluid Phase Equilib.* 487 (2019) 8–15.
- [45] L. Wang, K. Neeves, X. Yin, E. Ozkan, Experimental Study and Modeling of the Effect of Pore Size Distribution on Hydrocarbon Phase Behavior in Nanopores, *SPE Annual Technical Conference and Exhibition*, Society of Petroleum Engineers, Amsterdam, The Netherlands, 2014, pp. 15.
- [46] Y. Wu, T. Fan, S. Jiang, X. Yang, H. Ding, M. Meng, D. Wei, Methane adsorption capacities of the lower paleozoic marine shales in the Yangtze platform, South China, *Energy Fuels* 29 (2015) 4160–4167.
- [47] T. Zhang, G.S. Ellis, S.C. Ruppel, K. Milliken, R. Yang, Effect of organic-matter type and thermal maturity on methane adsorption in shale-gas systems, *Org. Geochem.* 47 (2012) 120–131.
- [48] F. Hao, H. Zou, Y. Lu, Mechanisms of shale gas storage: Implications for shale gas exploration in China, *AAPG Bull.* 97 (2013) 1325–1346.
- [49] Z. Li, Z. Jin, A. Firoozabadi, Phase behavior and adsorption of pure substances and mixtures and characterization in nanopore structures by density functional theory, *SPE J.* 19 (2014) 1096–1109.
- [50] A.G. Adesida, I. Akkutlu, D.E. Resasco, C.S. Rai, Characterization of Barnett Shale Kerogen Pore Size Distribution using DFT Analysis and Grand Canonical Monte Carlo Simulations, in: *SPE Annual Technical Conference and Exhibition*, Society of Petroleum Engineers, Denver, Colorado, USA, 2011.
- [51] U. Kuila, M. Prasad, Understanding pore-structure and permeability in shales, *SPE Annual Technical Conference and Exhibition*, Society of Petroleum Engineers, Denver, Colorado, USA, 2011.
- [52] Z. Jin, A. Firoozabadi, Thermodynamic modeling of phase behavior in shale media, *SPE J.* 21 (2016) 190–207.
- [53] K. Mosher, J. He, Y. Liu, E. Rupp, J. Wilcox, Molecular simulation of methane adsorption in micro- and mesoporous carbons with applications to coal and gas shale systems, *Int. J. Coal Geol.* 109–110 (2013) 36–44.
- [54] Y. Liu, J. Wilcox, Molecular simulation of CO₂ adsorption in micro- and mesoporous carbons with surface heterogeneity, *Int. J. Coal Geol.* 104 (2012) 83–95.
- [55] J. Rouquerol, D. Avnir, C. Fairbridge, D. Everett, J. Haynes, N. Pernicone, J. Ramsay, K. Sing, K. Unger, Recommendations for the characterization of porous solids (Technical Report), *pac* 66 (1994) 1739.
- [56] M. Alfi, H. Nasrabadi, D. Banerjee, Experimental investigation of confinement effect on phase behavior of hexane, heptane and octane using lab-on-a-chip technology, *Fluid Phase Equilib.* 423 (2016) 25–33.
- [57] J. Zhong, S.H. Zandavi, H. Li, B. Bao, A.H. Persad, F. Mostowfi, D. Sinton, Condensation in one-dimensional dead-end nanochannels, *ACS Nano* 11 (2017) 304–313.
- [58] J. Gross, A density functional theory for vapor-liquid interfaces using the PCP-SAFT equation of state, *J. Chem. Phys.* 131 (2009), 204705.
- [59] S. Tripathi, W.G. Chapman, Microstructure of inhomogeneous polyatomic mixtures from a density functional formalism for atomic mixtures, *J. Chem. Phys.* 122 (2005), 094506.
- [60] S. Tripathi, W.G. Chapman, Microstructure and thermodynamics of inhomogeneous polymer blends and solutions, *Phys. Rev. Lett.* 94 (2005), 087801.
- [61] C. Klink, J. Gross, A density functional theory for vapor-liquid interfaces of mixtures using the perturbed-chain polar statistical associating fluid theory equation of state, *Ind. Eng. Chem. Res.* 53 (2014) 6169–6178.
- [62] S. Jain, A. Dominik, W.G. Chapman, Modified interfacial statistical associating fluid theory: a perturbation density functional theory for inhomogeneous complex fluids, *J. Chem. Phys.* 127 (2007), 244904.
- [63] J. Liu, S. Xi, W.G. Chapman, Competitive sorption of CO₂ with gas mixtures in nanoporous shale for enhanced gas recovery from density functional theory, *Langmuir* 35 (2019) 8144–8158.
- [64] E.L. Camacho Vergara, G.M. Kontogeorgis, X. Liang, Gas adsorption and interfacial tension with classical density functional theory, *Ind. Eng. Chem. Res.* 58 (2019) 5650–5664.
- [65] G. Shen, X. Ji, S. Öberg, X. Lu, A hybrid perturbed-chain SAFT density functional theory for representing fluid behavior in nanopores: mixtures, *J. Chem. Phys.* 139 (2013), 194705.
- [66] E. Sauer, J. Gross, Classical density functional theory for liquid-fluid interfaces and confined systems: a functional for the perturbed-chain polar statistical associating fluid theory equation of state, *Ind. Eng. Chem. Res.* 56 (2017) 4119–4135.
- [67] E. Sauer, A. Terzis, M. Theiss, B. Weigand, J. Gross, Prediction of contact angles and density profiles of sessile droplets using classical density functional theory based on the PCP-SAFT equation of state, *Langmuir* 34 (2018) 12519–12531.

- [68] X. Xu, D.E. Cristancho, S. Costeux, Z.-G. Wang, Density-functional theory for polymer-carbon dioxide mixtures: a perturbed-chain SAFT approach, *J. Chem. Phys.* 137 (2012), 054902.
- [69] G. Shen, X. Lu, X. Ji, Modeling of molecular gas adsorption isotherms on porous materials with hybrid PC-SAFT-DFT, *Fluid Phase Equilib.* 382 (2014) 116–126.
- [70] C.P. Emborsky, Z. Feng, K.R. Cox, W.G. Chapman, Recent advances in classical density functional theory for associating and polyatomic molecules, *Fluid Phase Equilib.* 306 (2011) 15–30.
- [71] L. Ko, R. Loucks, S. Ruppel, T. Zhang, S. Peng, Origin and characterization of Eagle Ford pore networks in the south Texas Upper Cretaceous shelf, *AAPG Bull.* 101 (2017) 387–418.
- [72] C.H.S. Mark, E. Curtis, R.J. Ambrose, C.S. Rai, Microstructural investigation of gas shales in two and three dimensions using nanometer-scale resolution imaging microstructure of gas shales, *AAPG Bull.* 96 (2012) 665–677.
- [73] K. Liu, M. Ostadhassan, J. Zhou, T. Gentzis, R. Rezaee, Nanoscale pore structure characterization of the Bakken shale in the USA, *Fuel* 209 (2017) 567–578.
- [74] A.Z. Panagiotopoulos, Adsorption and capillary condensation of fluids in cylindrical pores by Monte Carlo simulation in the Gibbs ensemble, *Mol. Phys.* 62 (1987) 701–719.
- [75] L. Chen, L. Zuo, Z. Jiang, S. Jiang, K. Liu, J. Tan, L. Zhang, Mechanisms of shale gas adsorption: evidence from thermodynamics and kinetics study of methane adsorption on shale, *Chem. Eng. J.* 361 (2019) 559–570.
- [76] T.F.T. Rexer, M.J. Benham, A.C. Aplin, K.M. Thomas, Methane adsorption on shale under simulated geological temperature and pressure conditions, *Energy Fuels* 27 (2013) 3099–3109.
- [77] S. Whittaker, B. Rostron, C. Hawkes, C. Gardner, D. White, J. Johnson, R. Chalaturnyk, D. Seeburger, A decade of CO₂ injection into depleting oil fields: monitoring and research activities of the IEA GHG Weyburn-Midale CO₂ monitoring and storage project, *Energy Procedia* 4 (2011) 6069–6076.
- [78] E. Fathi, I.Y. Akkutlu, Multi-component gas transport and adsorption effects during CO₂ injection and enhanced shale gas recovery, *Int. J. Coal Geol.* 123 (2014) 52–61.
- [79] R. Bi, S. Luo, J. Lutkenhaus, H. Nasrabadi, Compositional Simulation of Cyclic Gas Injection in Liquid-Rich Shale Reservoirs Using Existing Simulators with a Framework for Incorporating Nanopores, in: *SPE Improved Oil Recovery Conference, Society of Petroleum Engineers, Tulsa, Oklahoma, USA, 2020*, pp. 21.
- [80] S. Luo, J.L. Lutkenhaus, H. Nasrabadi, Effect of nano-scale pore size distribution on fluid phase behavior of gas IOR in shale reservoirs, in: *SPE Improved Oil Recovery Conference, Society of Petroleum Engineers, Tulsa, Oklahoma, USA, 2018*, p. 14.
- [81] M.S. Wertheim, Fluids with highly directional attractive forces. I. Statistical thermodynamics, *J. Stat. Phys.* 35 (1984) 19–34.
- [82] M.S. Wertheim, Fluids with highly directional attractive forces. II. Thermodynamic perturbation theory and integral equations, *J. Stat. Phys.* 35 (1984) 35.
- [83] M.S. Wertheim, Fluids with highly directional attractive forces. III. Multiple attraction sites, *J. Stat. Phys.* 42 (1986) 459–476.
- [84] M.S. Wertheim, Fluids with highly directional attractive forces. IV. Equilibrium polymerization, *J. Stat. Phys.* 42 (1986) 477–492.
- [85] A. Dominik, S. Tripathi, W.G. Chapman, Bulk and interfacial properties of polymers from interfacial SAFT density functional theory, *Ind. Eng. Chem. Res.* 45 (2006) 6785–6792.
- [86] R. Evans, The nature of the liquid-vapour interface and other topics in the statistical mechanics of non-uniform, classical fluids, *Adv. Phys.* 28 (1979) 143–200.
- [87] Z. Li, A. Firoozabadi, Interfacial tension of nonassociating pure substances and binary mixtures by density functional theory combined with Peng-Robinson equation of state, *J. Chem. Phys.* 130 (2009), 154108.
- [88] J. Liu, L. Wang, S. Xi, D. Asthagiri, W.G. Chapman, Adsorption and phase behavior of pure/mixed alkanes in nanoslit graphite pores: an iSAFT application, *Langmuir* 33 (2017) 11189–11202.
- [89] J. Gross, G. Sadowski, Perturbed-chain SAFT: an equation of state based on a perturbation theory for chain molecules, *Ind. Eng. Chem. Res.* 40 (2001) 1244–1260.
- [90] Y.-X. Yu, J. Wu, Structures of hard-sphere fluids from a modified fundamental-measure theory, *J. Chem. Phys.* 117 (2002) 10156–10164.
- [91] Y.-X. Yu, J. Wu, Density functional theory for inhomogeneous mixtures of polymeric fluids, *J. Chem. Phys.* 117 (2002) 2368–2376.
- [92] Z. Jin, A. Firoozabadi, Thermodynamic modeling of phase behavior in shale media, *SPE J.* 21 (2016).
- [93] W.A. Steele, The physical interaction of gases with crystalline solids: I. Gas-solid energies and properties of isolated adsorbed atoms, *Surf. Sci.* 36 (1973) 317–352.
- [94] Y. Wang, N. Shardt, C. Lu, H. Li, J.A.W. Elliott, Z. Jin, Validity of the Kelvin equation and the equation-of-state-with-capillary-pressure model for the phase behavior of a pure component under nanoconfinement, *Chem. Eng. Sci.* 226 (2020), 115839.
- [95] J.P. Olivier, Modeling physical adsorption on porous and nonporous solids using density functional theory, *J. Porous Mater.* 2 (1995) 9–17.
- [96] Y. Kurniawan, S.K. Bhatia, V. Rudolph, Simulation of binary mixture adsorption of methane and CO₂ at supercritical conditions in carbons, *AIChE J.* 52 (2006) 957–967.
- [97] T. Pitakbunkate, T.A. Blasingame, G.J. Moridis, P.B. Balbuena, Phase behavior of methane-ethane mixtures in nanopores, *Ind. Eng. Chem. Res.* 56 (2017) 11634–11643.
- [98] A. Sharma, V. Luxami, K. Paul, Purine-benzimidazole hybrids: synthesis, single crystal determination and in vitro evaluation of antitumor activities, *Eur. J. Med. Chem.* 93 (2015) 414–422.
- [99] S. Wang, Q. Feng, F. Javadpour, Q. Hu, K. Wu, Competitive adsorption of methane and ethane in montmorillonite nanopores of shale at supercritical conditions: a grand canonical Monte Carlo simulation study, *Chem. Eng. J.* 355 (2019) 76–90.
- [100] T. Lee, L. Bocquet, B. Coasne, Activated desorption at heterogeneous interfaces and long-time kinetics of hydrocarbon recovery from nanoporous media, *Nat. Commun.* 7 (2016) 11890.